Biomaterials Advances 163 (2024) 213955

Contents lists available at ScienceDirect

Biomaterials Advances

journal homepage: www.journals.elsevier.com/materials-science-and-engineering-c

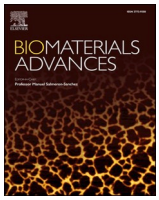

# Graded or random – Effect of pore distribution in 3D titanium scaffolds on corrosion performance and response of hMSCs

J. Idaszek [a,*], B. Wysocki [b], E. Ura-Bińczyk [a], A. Dobkowska [a], W. Nowak [b], A. Yamamoto [c], G. D. Sulka [d], W. Święszkowski [a]

[a] Warsaw University of Technology, Faculty of Materials Science and Engineering, Warsaw, Poland
[b] Cardinal Stefan Wyszynski University in Warsaw, Multidisciplinary Research Center, Dziekanow Lesny, Poland
[c] National Institute for Materials Science, Research Center for Macromolecules and Biomaterials, Tsukuba, Japan
[d] Jagiellonian University, Faculty of Chemistry, Department of Physical Chemistry and Electrochemistry, Gronostajowa 2, 30387 Krakow, Poland

ARTICLE INFO

*Keywords:*
Titanium
Laser beam powder bed fusion
Pore distribution
Corrosion
hMSC

ABSTRACT

Researchers agree that the ideal scaffold for tissue engineering should possess a 3D and highly porous structure, biocompatibility to encourage cell/tissue growth, suitable surface chemistry for cell attachment and differentiation, and mechanical properties that match those of the surrounding tissues. However, there is no consensus on the optimal pore distribution. In this study, we investigated the effect of pore distribution on corrosion resistance and performance of human mesenchymal stem cells (hMSC) using titanium scaffolds fabricated by laser beam powder bed fusion (PBF-LB). We designed two scaffold architectures with the same porosities (i.e., 75 %) but different distribution of pores of three sizes (200, 500, and 700 μm). The pores were either grouped in three zones (graded, GRAD) or distributed randomly (random, RAND). Microfocus X-ray computed tomography revealed that the chemically polished scaffolds had the porosity of 69 ± 4 % (GRAD) and 71 ± 4 % (RAND), and that the GRAD architecture had the higher surface area (1580 ± 101 vs 991 ± 62 $mm^2$) and the thinner struts (221 ± 37 vs 286 ± 14 μm). The electrochemical measurements demonstrated that the apparent corrosion rate of chemically polished GRAD scaffold decreased with the immersion time extension, while that for polished RAND was increased. The RAND architecture outperformed the GRAD one with respect to hMSC proliferation (over two times higher although the GRAD scaffolds had 85 % higher initial cell retention) and migration from a monolayer. Our findings demonstrate that the pore distribution affects the biological properties of the titanium scaffolds for bone tissue engineering.

## 1. Introduction

Tissue and organ failure caused by disease, injury, or developmental defects is a significant healthcare and economic issue [1]. The field of bone tissue engineering has led to new treatment methods for tissue and organ failures using growth factors, gene therapy, and cell transplantation, which support the regeneration process [2–4]. However, the regeneration of bone tissue defects, especially those of critical size and complex shape, remains a great challenge. To create the necessary space and structure for regenerating tissue, an artificial matrix, a scaffold, can be used. Recently, graded/gradient porous scaffolds that mimic natural bones morphologically and mechanically, have been developed for enhanced therapeutic effectiveness [5–8]. Such scaffolds allow to simultaneously match the mechanical properties of the implant to those of bone, and provide better osteointegration [9,10]. In the past, traditional methods like slurry foaming, gas foaming, and investment casting, were limited by a lack of accurate control over the shape, size, and distribution of pores, making it difficult to fabricate biomimetic graded/gradient scaffolds [11,12]. However, the advent of the additive manufacturing (AM) processes, e.g., laser beam powder bed fusion (PBF-LB), electron beam powder bed fusion (PBF-EB), and binder jetting (BJ), have addressed these challenges, enabling the fabrication of implants with complex structures [13–15]. The mentioned methods allow for the creation of implants using a variety of metallic materials, including popular titanium alloys [16,17], widely studied resorbable magnesium or iron alloys [18–20], and even metallic glasses [21,22]. Importantly, powder bed fusion using laser beam is considered the most promising of the aforementioned AM technologies for creating graded/gradient

* Corresponding author.
*E-mail address:* joanna.idaszek@pw.edu.pl (J. Idaszek).

https://doi.org/10.1016/j.bioadv.2024.213955
Received 22 February 2024; Received in revised form 3 July 2024; Accepted 5 July 2024
Available online 8 July 2024

porous structures due to its high precision [23–25].

The unprecedented control over the internal architecture of the scaffold, i.e., pore shape and size, or strut thickness, enables also tuning of the biological properties of the scaffolds. It is well established that different pore sizes influenced bone formation both in vitro and in vivo (described in [10,26,27]). The modulation of cell behaviour by pore size could also be applied to designing the graded/gradient scaffolds. For example, Onal and co-workers showed that the combination of a small-pore core with a big-pore outer shell provided the best proliferation of MC3T3-E1 pre-osteoblasts among all tested architectures [28]. Di Luca and co-workers showed that human mesenchymal stem cells (hMSC) differentiated better towards osteoblasts and chondrocytes when graded scaffolds were utilized [29–31]. In our previous studies, we have also demonstrated that graded scaffolds with the core made of small pores (200 μm) and shell made of big pores (500 μm) enabled high cell retention upon inoculation, and proliferation similar to that measured on homogenous scaffolds with 200 μm pores [7]. Another premise for application of bigger pores in outer regions of the graded scaffolds could be the results obtained by Taniguchi et al., who observed more advanced bone ingrowth into Ti PBF-LB scaffolds with pore sizes of 600 and 900 μm than of 300 μm [32]. However, all of the aforementioned scaffolds had pores of different sizes organized either in zones changing in a step-wise manner (graded scaffolds) or continuously (gradient scaffolds). To our best knowledge, there is no information available on the effect of random and organized pore distribution within AM-scaffolds with the same porosities on biological properties thereof.

Due to their envisioned long-term application, metallic implants have to also exhibit good corrosion resistance against biological environment such as exposure to bodily fluids [33]. This is even more important in case of porous 3D scaffolds, which have significantly higher surface-to-volume ratio than the bulk implants. We have previously reported that chemical polishing of 3D-printed Ti scaffolds in a mixture of acids containing oxidizing nitric acid leads to passivation of the surface by a layer of titanium oxides [8,34]. However, the effect of this process on corrosion resistance remains poorly investigated. Corrosion behaviour of scaffolds depends not only on chemical compositions and microstructure formed during fabrication, but also the kinetics of dissolution reactions are influenced by other factors, such as porosity, pore size and structure type. The structure determines flow of the solution inside the scaffolds which might play a crucial role in its corrosion reactions (change of pH during application, exchange of released ions). Łosiewicz et al. investigated corrosion of pure Ti cellular lattice with various architectures of triply periodic minimal surfaces (TPMS) in an alkaline solution, and they obtained the lowest corrosion rate for the architecture with the smallest surface area [35]. Recently, Puttonen et al. reported the influence of the size and shape of gyroid- and daimon-cell structures on their corrosion performance, and that localized corrosion was a predominant mechanism [36]. Unfortunately, they were not able to measure the corrosion rate accurately due to negligible mass loss of the samples or insufficient cleaning of corrosion products after immersion. Because of stochastic nature of corrosion, the effect of pore distribution on the corrosion resistance of Ti scaffolds remains unexplored, and there is no data regarding the influence of pore distribution in the scaffold's architecture on its corrosion response.

Since graded/gradient porous structures may reflect natural variation in bone density, it is important to investigate how various scaffold architectures, specifically, the size and the distribution of pores, affect their corrosion and biological properties. Therefore, the aim of this study is to investigate the effect of pore distribution in scaffolds with the same porosity on their corrosion behaviour and the performance of hMSC. To this end, we designed two types of scaffold architectures consisting of pores with sizes of 200, 500 and 700 μm. These pores were distributed either randomly throughout the scaffold or grouped into three zones, with pore size increasing from core zone (200 μm) towards the outer zone (700 μm). Ti scaffolds were fabricated using PBF-LB and subjected to chemical polishing. Following characterization of surface by means of scanning electron microscopy and porosity by means of microfocus X-ray computed tomography, the corrosion properties of the scaffolds were investigated using electrochemical measurements, i.e., potentiodynamic polarization and electrochemical impedance spectroscopy. Finally, the scaffolds were employed for inoculating hMSC using cell suspension and cell monolayer, and the effect of the scaffolds architecture on cell retention, distribution, colonization, proliferation, and osteogenic differentiation was evaluated.

## 2. Materials and methods

### 2.1. Scaffolds design

Scaffolds used in this study were designed with two architectures, resulting in an open porosity of 75 %. Both architectures were composed of pores with the dimension of 200, 500 and 700 μm; however, they varied in distribution of pores. The pore size in the range of 200–700 μm would promote both cell colonization and vascularization [15,37]. The architectures of both scaffolds are schematically shown in Fig. 1. The first architecture was composed of the pores arranged in zones (labelled as graded scaffold, Fig. 1A), while the second one consisted of randomly distributed pores (Fig. 1B). The graded architecture of scaffold was designed using Magics Materialise 26.01 software, employing the Magics Structures module and Boolean operations. Graded scaffolds were designed by filling three scaffold zones (R1: core, R2: intermediate region and R3: shell) using custom-designed diamond elemental cells. Different sizes of diamond structures resulted in pores of 200 μm (R1), 500 μm (R2) and 700 μm (R3). Each of the zones was made with an additional 100 μm offset to ensure a good connection between the regions (see Fig. S1). The Laguerre–Voronoi tessellations were used to design scaffolds with a random 200, 500, and 700 μm pore distribution. These scaffolds had pore shapes close to spherical. The detailed procedure of designing open cell structures using Laguerre–Voronoi tessellations was described in our previously published articles [38,39]. The exact scaffold dimensions are summarized in Table 1 and in Fig. 1.

### 2.2. Laser beam powder bed fusion (PBF-LB)

The scaffolds used in this study were created through PBF-LB technology using a Realizer SLM50 (Realizer GmbH/DMG Mori in Borchen, Germany) metal additive manufacturing machine. The scaffolds were made from gas-atomized, spherical (diameter below 45 μm) commercially pure (CP) Ti Grade 1 (TiGr1) powder provided by ECKART TLS (Bitterfeld-Wolfen, Germany.) The manufacturer's information confirms that the powder meets ISO/ASTM TiGr1 requirements, with a purity of at least 99.5 % (*w*/w) (max. 0.20 % Fe, max. 0.08 % C, max. 0.03 % N, max. 0.015 % H, max. 0.18 % O, balance Ti). To ensure no damage of the delicate scaffold struts and facilitate the removal of the scaffold from the support and building platform, higher energy density was delivered to the main part (scaffold) than to its support structure [40]. The main part was created using parameters from a previous study, which included a laser power of 42 W and a scanning speed of 375 mm/s, with a layer thickness of 25 μm [8]. The laser scanning strategy for the main part alternated with a 45° rotation on each layer, while keeping 30 μm distance between each laser scanning vector (hatch distance). For the main part (scaffold), the PBF-LB process summarized energy density was 150 J/mm$^3$. The support structure for the main part was created using a lower laser power (30 W) with the same exposure time (40 μs) at each random point of the support structure's cross-section. Using a lower laser power for the support structure helped make the support structure easier to remove by hand. The scaffolds were created in an inert argon atmosphere, and the oxygen level ranged between 0.2 and 0.4 vol% to enhance the material's strength through a solid solution strengthening mechanism [41,42]. The detailed parameters and architecture of support structures were described in our previous study [40].

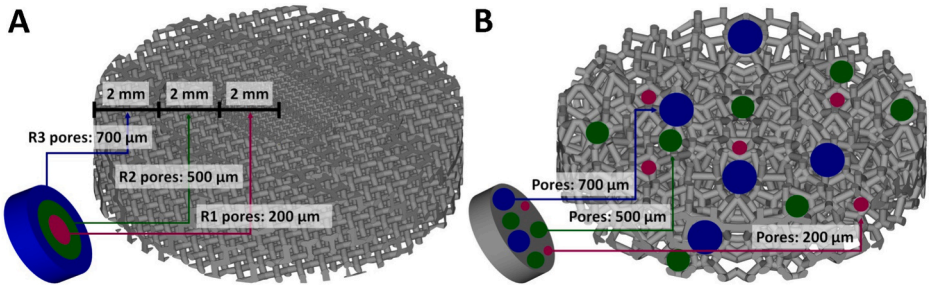


**Fig. 1.** CAD models of (A) the graded scaffold with the indicated zones containing pores with sizes of 200 µm, 500 µm, and 700 µm, and (B) the scaffold with a random distribution of the pores with sizes of 200, 500, and 700 µm.

**Table 1**
Comparison of CAD models of graded and random scaffolds.

| Scaffold type/pore distribution | Dimensions [mm] | Volume [$mm^3$] | CAD open porosity [%] | Pore size [µm] | Surface area [$mm^2$] | Strut diameter [µm] | Cell type |
|---|---|---|---|---|---|---|---|
| Graded | d = 12, h = 3 | 71 | 75 | R1: 200<br>R2: 500<br>R3: 700 | 1437 | R1: 100<br>R2: 190<br>R3: 230 | Diamond |
| Random | d = 12, h = 3 | 72 | 75 | 200<br>500<br>700 | 998 | 260 | – |

### 2.3. Scaffolds chemical post-processing

To ensure the removal of the unmelted powder particles from the scaffold interior, we have used the chemical polishing process in the HF/$HNO_3$ acids solution. This process also helped improve CAD accuracy and remove the support structure residues after manual detaching [43]. The details of this procedure can be found in references [7,8]. Briefly, the scaffolds were firstly immersed multiple times in distilled water to remove any non-melted powder particles and clear open spaces in the scaffold structures. Then, the scaffolds were polished in an ultrasonic cleaner using a solution of HF/$HNO_3$. Unlike the main part, all unmelted powders and support residues were dissolved without damaging the scaffold struts due to the lower energy density delivered to the support structures. The HF/$HNO_3$ acids used in this study had a concentration of 2.2 % HF/20 % $HNO_3$, and the immersion time was 6 min, following a patented procedure [44].

### 2.4. Scanning electron microscopy (SEM) and microfocus X-ray computed tomography (µCT)

The PBF-LB fabricated scaffolds were examined using a Thermo Scientific™ Axia™ ChemiSEM™ Scanning Electron Microscope (SEM). The architecture and surface of the struts in the chemically polished and unpolished scaffolds were observed in Secondary Electron (SE) mode, with an accelerated voltage of 20 kV.

The µCT scans were performed on three representative chemically polished graded and random scaffolds using a Nikon XT H 225 ST 2× scanner equipped with the multi-metal target (tungsten used in our study). The source voltage and source current were set to 160 kV and 34 µA, respectively. A 0.5 mm aluminium filter material was chosen to obtain the optimum greyscale value for the reconstruction. The scanning procedure was made by performing 1000 projections and 32 frames per projection, with an exposure time of 67 ms. The reconstructed voxel size was set to 5.5 µm. The reconstruction data were prepared using Nikon CT Pro 3D software, and data visualisation and porosity measurements were performed by Volume Graphics Studio Max 2022.3 with an Additive Manufacturing set of plugins.

### 2.5. Electrochemical studies

The electrochemical measurements included monitoring of open circuit potential for 2 h, followed by potentiodynamic polarization. The tests were performed in a quiescent phosphate buffered saline (PBS) solution at 37 °C using an Autolab PGSTAT302N potentiostat/galvanostat (Methrom). The PBS was prepared from chemically pure reagents and distilled water (8 g/l NaCl, 0.2 g/l KCl, 1.44 g/l $Na_2HPO_4$, 0.24 g/l $KH_2PO_4$) with pH adjusted to 7.4 with HCl. A standard three-electrode setup with a platinum plate as a counter electrode, a silver chloride electrode ($Ag|AgCl|KCl_{sat}$) as a reference electrode, and a scaffold as a working electrode, was used. The potentiodynamic polarization was registered after 2 h of immersion, with a 1 mV/s scan rate, starting from 200 mV below the open circuit potential ($E_{OCP}$). The scan was stopped at the potential of 2 $V_{Ag|AgCl}$. The corrosion current density ($i_{corr}$) and corrosion potential ($E_{corr}$) were calculated using the Tafel extrapolation method. The scaffold surface area obtained by µCT observation was applied as the surface area of the working electrode. The large-volume electrochemical cell was used with the ratio of solution to the surface area of the working electrode over 100 ml/$cm^2$. To ensure the reproducibility of the results, three scaffolds were tested for each of the specific architecture, both with and without chemical polish (including as-made graded scaffolds, as-made random scaffolds, chemically polished graded scaffolds, and chemically polished random scaffolds). The electrochemical impedance spectroscopy (EIS) was recorded after 2 and 72 h of immersion in PBS at 37 °C. EIS was performed with AC amplitude of 10 mV at a frequency range 0.01 to 10,000 Hz with 10 points per decade. The measurements and equivalent circuit fitting of the electrochemical data were performed using NOVA 2.0 software.

### 2.6. Cell culture

Bone-marrow derived hMSC were purchased from Lonza Walkersville (USA) and cultured in an expansion medium, i.e., α-MEM (alpha modified Eagle Minimum Essential Medium) supplemented with 10 % (*v*/v) of foetal bovine serum (FBS, EuroClone, Italy), 1 % (v/v) of penicillin and streptomycin (PS, Gibco, UK) and 1 ng/ml of FGF2 (Sigma-Aldrich, Israel). For osteogenic differentiation of hMSCs, a differentiation medium was used. This medium included α-MEM supplemented with 10 % (v/v) of FBS, 1 % (v/v) of PS, 50 µg/ml of ascorbic

acid phosphate (Sigma, Japan), 10 mM β-glycerophosphate (Sigma, USA), 10 nM 1,25-dihydroxy-vitamin D3 (Sigma, Israel) and 10 nM of dexamethasone (Sigma, China).

Ti scaffolds were sterilized by immersion in 70 % ethanol, followed by three washes with Dulbecco's phosphate buffered saline (PBS, Sigma, UK) and an overnight incubation in expansion medium. Only chemically polished scaffolds were used in the cell culture experiments due to their superior biocompatibility, as confirmed in our previous study [8].

### 2.7. Cell seeding

The hMSC from passage 4 were seeded onto the scaffolds at density of $2 \times 10^5$ cells per scaffold in a 10 μl droplet. After allowing the cells to adhere for 2 h, we added the expansion medium. Following an overnight incubation at 37 °C under 5 % $CO_2$ in air and ~90 % relative humidity, the inoculated samples were transferred into new wells containing the differentiation medium and cultured up to 35 days. The medium was changed every 2–3 days.

### 2.8. Colonization of the scaffolds by hMSC migrating from a monolayer

The monolayer of hMSC was prepared by seeding the cells on a silicone sheet [45]. Briefly, silicone sheets were placed on Teflon substrates, autoclaved and left to dry in a laminar flow cabinet. On the next day, the samples were treated with nitrogen plasma (30 W, $N_2$ flow = 0.5 l/h, $p = 0.75$ mbar) for 30 s. These treated samples were then placed in wells of 6-well plates, to which 4 ml of the expansion medium was added. Approximately 4 h later, hMSC were added dropwise ($3.5 \times 10^5$ cells per well, 1 ml of the expansion medium) and cultured for 1 day. Subsequently, the sheets were placed on the investigated scaffolds with the cell-seeded side facing the scaffolds, and cultured for 14 days in the differentiation medium. After that period, six scaffolds of each architecture were fixed with a solution of 4 % paraformaldehyde (PFA, Sigma-Aldrich, Germany) in PBS (Sigma, USA) for 1 h, stained with DiI (1,1′-Dioctadecyl-3,3,3′,3′-Tetramethylindocarbocyanine Perchlorate, Molecular Probes, USA) for 15 min at room temperature (RT), washed, and visualized using a fluorescent microscope (Leica TCS SP8) with excitation at $\lambda = 530 \pm 10$ nm and emission at $\lambda = 570 \pm 10$ nm. The remaining samples were used to perform MTS, DNA, and alkaline phosphatase (ALP) assays (as described in the following Sections 2.9–2.11).

### 2.9. Viability of hMSC

The viability of hMSC seeded onto the scaffolds was investigated qualitatively by live/dead staining. At predetermined time points, cells were washed with PBS and treated with 1 ml of the live/dead stain containing 3 μg/ml of acridine orange (*N*,*N*,*N*′,*N*′-tetramethylacridine-3,6-diamine, Sigma, USA), which stains all cells green, and 10 μg/ml of ethidium bromide (3,8-diamino-5-ethyl-6-phenylphenanthridinium bromide, Sigma, India), which stains dead cells red. After 5 min of incubation at RT, the scaffolds were washed with PBS and observed using a fluorescent microscope (Leica TCS SP8) with filter sets corresponding to the fluorochromes of interest.

To quantify the viability of the cells migrating into the scaffolds from a monolayer, we performed the MTS assay. First, the scaffolds were washed with α-MEM medium w/o FBS. Next, they were moved to wells of a 24-well plate containing 1 ml of α-MEM w/o FBS, to which 200 μl of MTS reagent ([3-(4,5-dimethylthiazol-2-yl)-5-(3-carboxymethoxyphenyl)-2-(4-sulfophenyl)-2H-tetrazolium], CellTiter 96® AQueous One Solution Cell Proliferation Assay, USA) was added. After incubating in a cell culture incubator for 90 min, the scaffolds were removed from the wells, and 4 × 100 μl of the remaining reaction mixture was transferred into a 96-well plate. Finally, the absorbance was measured at $\lambda =$ 490 nm.

### 2.10. DNA assay

The DNA assay was performed to determine changes in DNA content over the culture period. At predetermined time points, the scaffolds were washed with PBS, transferred to new wells containing sterile deionized water, and lysed using three freezing-thawing-intense pipetting cycles. The resulting lysate (4 × 100 μl) was then used to quantify DNA content using CyQuant™ proliferation assay (Thermo Fisher Scientific, USA) following the protocol provided by the manufacturer.

### 2.11. Osteogenic differentiation of hMSC

#### 2.11.1. Alkaline phosphatase (ALP) activity

The lysate (4 × 100 μl) collected above was combined with an equal volume of *p*-nitrophenyl phosphate (pNPP, ALP substrate, Thermo Fisher Scientific, USA) and incubated at RT for 1 h. The absorbance was measured at $\lambda = 405$ nm, and the concentration of the *p*-nitrophenol (pNP) was calculated based on a standard curve prepared in advance. The conversion of pNPP into pNP was then normalized to the total DNA content measured by the DNA assay.

To visualize the expression of ALP, the cells were fixed on days 7 and 14 using 4 % PFA. After permeabilization with 0.1 % Triton X-100 for 15 min, non-specific binding was blocked by incubating the samples in 10 % goat serum for 30 min. Next, the samples were incubated with a primary antibody (monoclonal mouse anti-bone ALP, GeneTex, 10 μg/ml) at 4 °C overnight, followed by a secondary antibody (Alexa Fluor 488 goat anti-mouse IgG, Invitrogen, diluted 1:300) at RT for 2 h. Finally, nuclei were stained with Draq5 (1:1000, Thermo Scientific) at RT for 15 min. After three washes with PBS, the samples were visualized using a confocal microscope (Leica TCS SP8) with excitation wavelengths of 488 nm and 633 nm.

#### 2.11.2. Mineralization

Cells in the scaffolds cultured for 28 and 35 days in the differentiation medium were fixed with 4 % PFA for 1 h, followed by three washes with deionized (DI) water. Subsequently, the cells were incubated in Alizarin Red S (3,4-Dihydroxy-9,10-dioxo-9,10-dihydroanthracene-2-sulfonic acid, ARS, Sigma-Aldrich, China) solution (40 mM, pH 4.1) for 1 h, and washed with DI water until the water became clear. The scaffolds were then transferred to new wells, and 0.5 ml of 10 % (*w/v*) solution of cetylpyridinium chloride (1-hexadecylpyridinium chloride, Sigma-Aldrich, USA) in 10 mM sodium phosphate (pH 7.0) was added to extract the ARS (1 h, 100 rpm). The resulting extracts (100 μl) were transferred in quadruplicate into a 96-well plate, and the absorbance was measured at $\lambda = 562$ nm [46].

Due to poor visibility of the mineralization nodules on the Ti samples [47], we decided to perform additional staining using xylenol orange. The staining procedure followed the method described by Wang and co-authors [48]. Briefly, the samples were incubated in aqueous solution of xylenol orange tetrasodium salt (200 mM, Merck) overnight and observed using a fluorescent microscope (Leica TCS SP8) with filter set corresponding to the fluorochrome of interest (excitation at $\lambda = 530 \pm$ 10 nm and emission at $\lambda = 570 \pm 10$ nm).

### 2.12. Statistics

The results are presented as a mean ± standard deviation (SD). The results were evaluated statistically by means of post hoc one-way ANOVA with a Tukey–Kramer pair-wise comparison test (KyPlot 2.0 beta 15 software).

## 3. Results

### 3.1. Scanning electron microscopy (SEM) and microfocus X-ray computed tomography (μCT)

The SEM observations of investigated scaffolds are shown in Fig. 2. Obviously, the surface of the scaffolds after fabrication was more developed due to the presence of the unmelted powder particles (Fig. 2A and C). The surface of the struts after chemical polishing was smoother, and no unmelted powder particles were observed (Fig. 2B and D). Chemical polishing resulted in the removal of unmelted powder particles from both types of architectures without compromising strut integrity. Furthermore, we did not observe any cracking or severe corrosion pitting due to chemical post-processing.

The μCT reconstructions of the scaffolds and their cross-sections are shown in Fig. 3. Thanks to the chemical polishing, there were almost no visible unmelted powder particles on the scaffold's struts, even in the regions of the smallest (200 μm) pores in both types of scaffolds.

After chemical polishing, both the graded and the random scaffolds exhibited porosity of 69 ± 4 % and 71 ± 4 %, respectively, closely matching those of the CAD models (see Table 1). The surface area of both architectures was also close to corresponding CAD models due to the removal of unmelted powder particles during the chemical polishing. As a result of a higher number of pores below the size of 200 μm and in the range of 200–500 μm (see Fig. 4), the surface area of the graded architecture was slightly higher after the PBF-LB process than that of the corresponding CAD model. The surface area-to-volume ratios (SA/V) of the graded and random scaffolds were 14.5 ± 5.9 and 11.3 ± 0.6 $mm^{-1}$, respectively. The parameters of the fabricated scaffolds obtained by means of the μCT are summarized in Table 2.

Following PBF-LB fabrication and chemical polishing, the dominant (above 60 %) pore size was in the range of 200–500 μm for graded architectures and above 500 μm for random architectures (as shown in Fig. 4). Most of the small pores closed during the PBF-LB fabrication process due to a relatively high energy density of fabrication.

### 3.2. Corrosion properties

The results obtained from the electrochemical tests performed in PBS at 37 °C are presented in Fig. 5. The internal architecture of scaffolds and chemical polishing clearly affected the corrosion behaviour of scaffolds. Lower values of the open circuit potential ($E_{OCP}$) were registered for both types of as-made scaffolds compared to those of the chemically polished ones. The lowest $E_{OCP}$ was observed for the as-made scaffolds with the graded architecture (Fig. 5a). At the beginning of immersion, the $E_{OCP}$ for this scaffold suddenly decreased from −0.07 V to −0.25 V vs Ag/AgCl, and reached the stable value of −0.27 V vs Ag/AgCl after approximately 45 min of immersion. A similar decreasing trend of $E_{OCP}$ was observed for the as-made scaffold with randomly distributed pores; the $E_{OCP}$ immediately decreased from −0.05 to −0.15 V vs Ag/AgCl during the first 20 min of immersion, and afterwards, a slightly decreasing trend was observed, reaching −0.18 V vs Ag/AgCl at the end of the measurement. The chemical polishing caused a shift of $E_{OCP}$ towards the nobler potentials. The most stable and the highest value of −0.06 V vs Ag/AgCl was measured for the chemically polished scaffold with the graded architecture. The $E_{OCP}$ of the chemically polished scaffold with random architecture was slightly lower, starting at −0.15 V and increasing towards −0.07 V vs Ag/AgCl after approximately 45 min of immersion.

The trend of the polarization curves recorded for the as-made scaffolds was similar and indicated their active behaviour (Fig. 5b). The chemical polishing changed the corrosion mechanism from active dissolution to passivation. On the anodic branch of the polarization curves, the current plateau occurred, which indicated the formation of a passive oxide film on the surface of the chemically polished scaffolds. It caused the shift of the polarization curves towards lower current densities, giving the significant decline in corrosion current density (Table 3). The scaffolds with random architecture had the higher $E_{corr}$ than that of the graded scaffolds in both conditions; as-made or chemically polished.

To further elucidate the influence of pore characteristics on the passive film property, the EIS data was fitted with the equivalent electric circuits presented in Fig. 6E. In the selected circuits, $R_s$ represents the resistance of the electrolyte, $R_{ct}$ is the resistance of the electric-charge transfer through the material and electrolyte interface, while $CPE_{ct}$ describes the properties of the double layer at the material-electrolyte interface [49,50]. $CPE_{ct}$ replaces an ideal capacitor and is described by $Y_{ct}$ (capacitance) and $a_1$ (dispersion coefficient). In the case of chemically polished graded scaffolds, two additional elements were added to the electronic equivalent circuit; $R_f$ and $C_f$ characterize the passive layer; the first variable represents the resistance of the passive film, while the second describes the capacitance of the passive layer [50].

The Nyquist plots exhibited incomplete and distorted capacitive semicircles, and the amplitude of semicircles after chemical polishing significantly increased (Fig. 6A and Fig. 6C). This confirmed that the chemical polishing significantly improved corrosion resistance of the scaffolds regardless of their architecture. An important observation is that in the case of the as-made scaffold with random architecture, the charge transfer resistance $R_{ct}$ increased with the extended time of immersion, whilst for the as-made graded scaffold, $R_{ct}$ decreased (Table 4). When analysing the behaviour of the polished scaffold with random

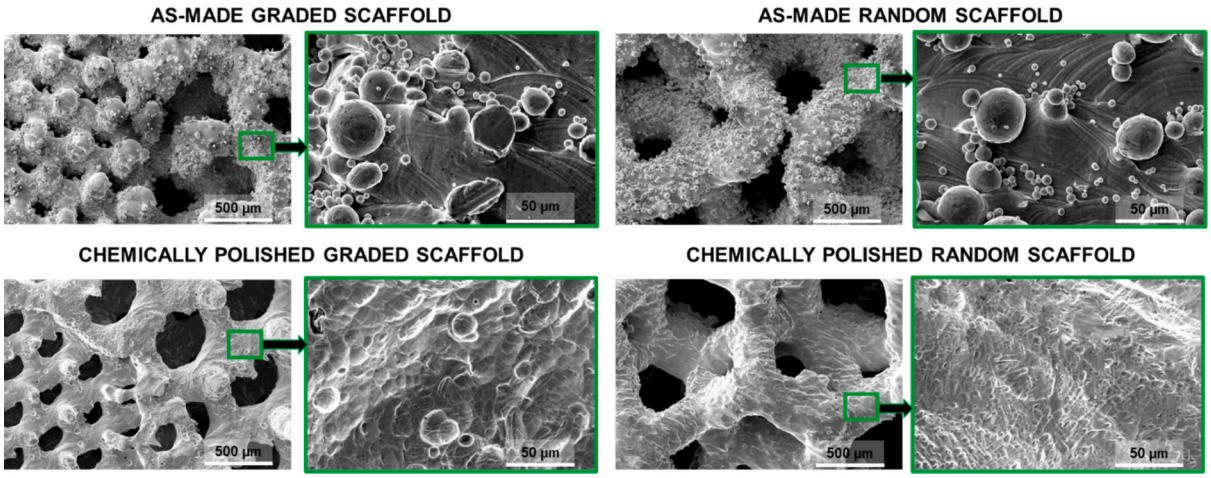


**Fig. 2.** SEM images of as-made (A, C) and chemically polished (B, D) graded scaffold (A, B) and random scaffold (C, D).

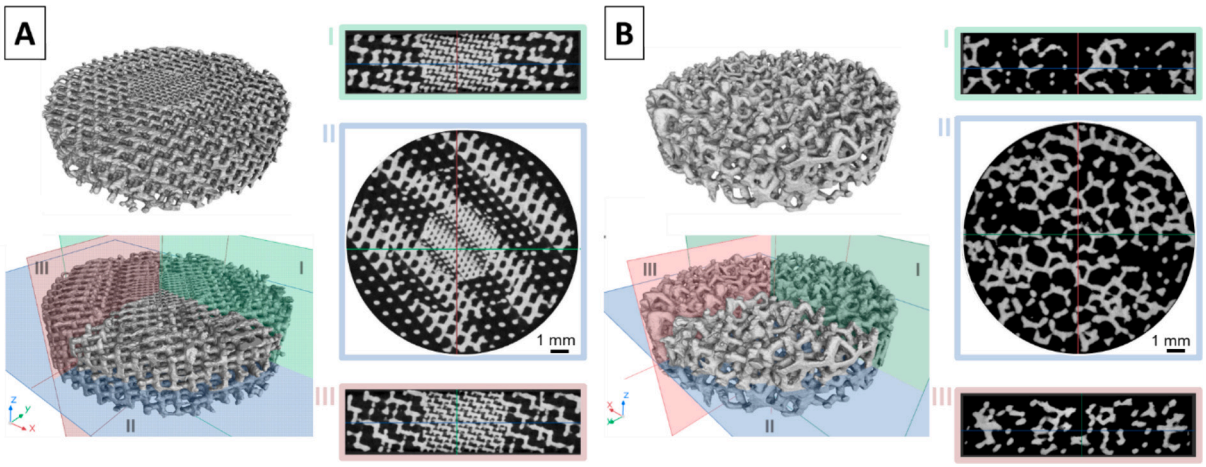


**Fig. 3.** The 3D μCT reconstruction of chemically polished (A) graded scaffold and (B) random scaffold.

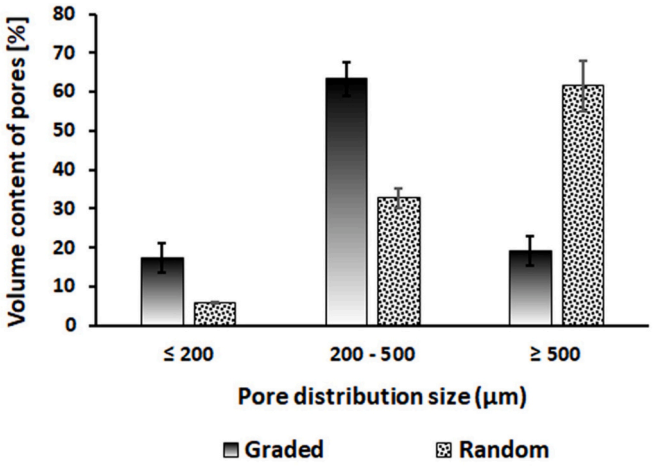


**Fig. 4.** Pore volume content in random and graded scaffold architectures.

**Table 2**
Comparison of the main parameters describing scaffolds with both designed architectures obtained by μCT.

| Scaffold type | PBF-LB open porosity [%] | PBF-LB strut diameter [μm] | PBF-LB surface area [$mm^2$] | PBF-LB volume [$mm^3$] | PBF-LB area/ volume [$mm^{-1}$] |
|---|---|---|---|---|---|
| Graded | 69 ± 4 | 221 ± 37 | 1580 ± 101 | 109 ± 17 | 14.5 ± 5.9 |
| R1 (core) | 49 ± 10 | 178 ± 16 | 380 ± 12 | 22 ± 3 | 17.9 ± 2.6 |
| R2 (core/ shell) | 73 ± 9 | 227 ± 16 | 567 ± 43 | 36 ± 5 | 16.0 ± 1.3 |
| R3 (shell) | 72 ± 4 | 258 ± 17 | 706 + 64 | 50 ± 8 | 14.3 ± 1.1 |
| Random | 71 ± 4 | 286 ± 14 | 991 ± 62 | 88 ± 6 | 11.3 ± 0.6 |

architecture, its $R_{ct}$ decreased with the extension of immersion time, indicating weakening of the passivation processes. The passivation mechanism of the graded scaffold after chemical polishing was different from that observed for the scaffold before chemical polishing and for the scaffolds with random architecture. In the former case, two time constants were well distinguishable (Fig. 6B and Fig. 6D). This strongly suggests that scaffolds' architecture had a critical influence on its passivation behaviour. The chemically polished scaffold with graded architecture changed the kinetics of the passivation processes, leading to intense growth of the passive film with the extended immersion time. This was confirmed by the increase in $R_{ct}$ and $R_f$ shown in Table 4. The EIS fitting showed that after 2 h of immersion, a higher radius of Nyquist plot was recorded for the scaffolds with random architecture. However, after 72 h, the reverse dependence was observed. The simplest approach to accurately determine the corrosion rate of the analysed scaffolds is to calculate total polarization resistance $R_p$ using data from simulated EIS spectra [51]. Knowing that a corrosion rate inversely scales with $R_p$ [52,53], the apparent corrosion resistance of the scaffolds after 2 h of immersion followed the order: as-made random and as-made graded architectures << chemically polished graded architectures < chemically polished random architectures. After 72 h, the corrosion resistance of the scaffolds changed as follows: as-made graded architectures < as-made random architectures << chemically polished graded architectures < chemically polished random architectures (Table 5).

### 3.3. Evaluation of biological performance

#### 3.3.1. HMSC viability, proliferation and differentiation (cell suspension)

Using cell suspension method, hMSC were seeded onto the scaffolds and remained viable, with virtually no dead (red) cells throughout the entire culture period (as shown in Fig. 7). The differences in pore distribution affected the cellular distribution. High cell density areas were visible on the top surface of the R1 zone in the graded scaffolds (which have the smallest pores) one day after seeding. In contrast, cell density on the top surface from R2 to R3 zones (with the medium and large pores) resembled that on the random scaffolds. On the other hand, the areas of higher cell density were observed in the lower layers of the random scaffolds and R3 zone of the graded scaffolds (visible in Fig. 7 as blurry green areas). Over the first week of the culture, cell density increased significantly in the core and intermediate zones of both the graded and random scaffolds, with cells bridging the struts and spreading across some pores. After two weeks of culture, hMSC closed pores on the top surface of the R1 zone and most of the pores in the R2 zone of the graded scaffolds. Interestingly, more cells were visible in the outer region of the random scaffolds compared the graded ones. By day 28 and 35 of culture, the cell density increased further, especially in the R3 region of the graded scaffolds.

The architecture of the scaffolds also influenced cell retention during seeding and proliferation in culture. Total DNA content was nearly twice as high (statistically significant) on the graded scaffolds compared to the random ones at 1-day post-seeding (see Fig. 8A). However, this difference was not apparent when considering surface area available for cell growth (see Fig. 8B). DNA concentration increased over the 2-week culture period but the significant increase was observed only on the

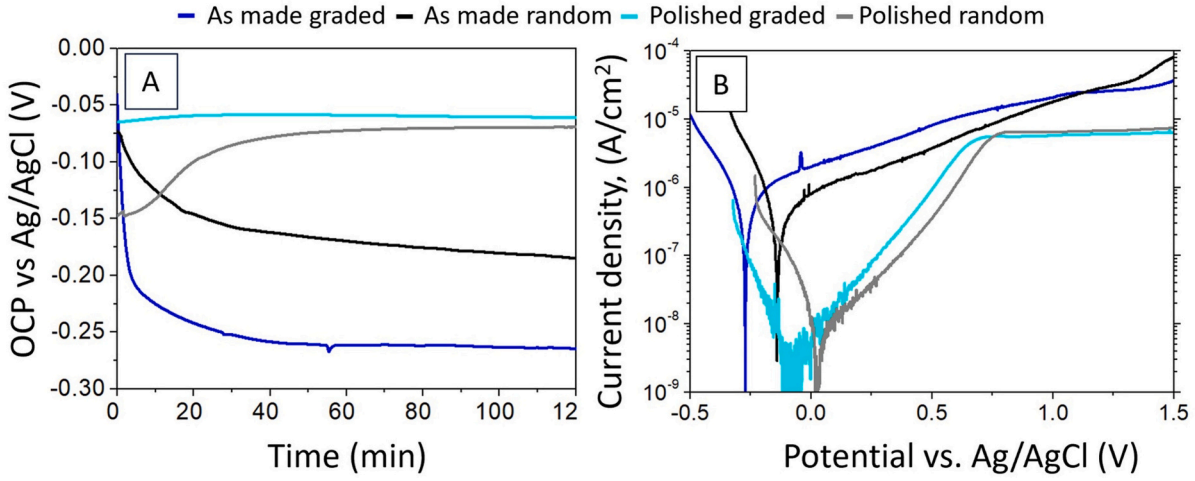


**Fig. 5.** Results of the electrochemical tests performed in PBS at 37 °C: a) open circuit potential ($E_{OCP}$), b) potentiodynamic curves.

**Table 3**
Electrochemical parameters obtained from the polarization curves shown in Fig. 5b using polarization resistance fitting; the standard deviation in the $E_{corr}$ values was within 20 mV ($i_{corr}$ – corrosion current density, $E_{corr}$ – corrosion potential).

| Scaffold | $i_{corr}$ (nA/cm$^2$) | $E_{corr}$ (V/Ref) |
|---|---|---|
| As made graded | 387 | −0.27 |
| Polished graded | 9 | −0.11 |
| As made random | 320 | −0.07 |
| Polished random | 9 | 0.02 |

random scaffolds between day 1 and day 7 (Fig. 8A; DNA concentration at day 7 was 142 % higher than on day 1). On the other hand, hMSC proliferation was significantly greater on the random scaffolds when normalized to the scaffold surface area (see Fig. 8B) and also when normalized to the initial DNA content (Fig. 8C).

Regarding the ALP activity, a significant (over 5–6 fold) increase was measured during the first week of culture for both graded and random scaffolds (see Fig. 8D); however, the pore distribution did not affect it. On the other hand, when normalized to the scaffold surface area, the ALP activity was significantly lower on the graded scaffolds at every time point compared to the random ones (Fig. 8E). ALP-positive cells were localized in areas of lower cell density, specifically, in R2 and R3 zone of the graded scaffolds and in the intermediate and outer regions of the random scaffolds (Fig. 8F). Additionally, more ALP-expressing cells were found in the centre of the random scaffolds than the graded ones.

The mineralization was relatively poor at both day 28 and 35 of osteogenic differentiation (Fig. 8G). After normalizing to the scaffold surface area, mineralization was significantly higher on the random scaffolds at day 28 (Fig. 8H); however, this difference diminished after additional week of osteogenic culture. To visualize the calcium deposits, we performed additional staining using a fluorescent dye, as conventional observations of mineralized nodules on Ti samples are challenging [47]. The staining correlated with the presence of ALP-positive cells at day 7 and 14, mainly occurring in the outer regions of the scaffolds (Fig. 8I).

#### 3.3.2. *Colonization of the scaffolds (migration from the hMSC monolayer)*

Images of fluorescently-labelled hMSC, which migrated to both the graded and random scaffolds after 2 weeks of culture, are depicted in Fig. 9. The pore distribution of the scaffolds did not affect the colonization of hMSC on the top surface of the scaffolds (Fig. 9 A and B), which was in direct contact with the cells growing on the silicone sheet. However, migration of hMSC through the graded scaffolds was hindered in the R1 zone and, to some extent, in the R2 zone, as confirmed by the less fluorescence at the bottom surface of the scaffolds (Fig. 9C). On the other hand, the hMSC managed to colonize the entire volume of the random scaffolds, as evidenced by the presence of cells on the bottom surface (Fig. 9 D).

To analyse the colonization quantitatively, we measured the DNA content. As shown in Fig. 10A, there was no significant difference between the two types of scaffolds. The same trend was confirmed for metabolic activity determined by the MTS assay (Fig. 10C) and ALP activity (Fig. 10E). However, when normalized to the scaffold surface area, the random scaffolds outperformed the graded ones (Fig. 10 B, D and F). The DNA concentration, MTS conversion, and ALP activity of the random scaffolds were 1.6–1.7 times higher than those of the graded ones (all statistically significant).

## 4. Discussion

### 4.1. *Accuracy in the scaffold fabrication*

In the present study, we have investigated the effect of pore distribution in scaffolds fabricated by PBF-LB on their corrosion and biological properties. The PBF-LB process, followed by the chemical polishing in the $HF/HNO_3$ acids, allowed the fabrication of scaffolds with a porosity of 69 ± 4 % and 71 ± 4 % for the graded and random architectures, respectively. Although this value was 4–6 % lower than the assumed porosity of 75 %, it was still very close to the assumptions of the CAD models. To the best of the authors' knowledge, obtaining fabrication with such high accuracy from the CAD models for bone scaffolds with strut sizes between 100 and 260 μm has not been reported before. Upon analysing the accuracy of the fabrication from the CAD model for the graded architecture, the lowest porosity of 49 ± 10 % and the strut size nearly 1.8 times thicker than that in the CAD model were observed for R1 of the fabricated scaffold (see Tables 1 and 2). Our results clearly showed that the energy level of 150 J/mm$^3$ was too high to achieve high dimensional accuracy for 100 μm diameter struts in R1, but it was acceptable for struts above 200 μm diameter. The porosity of R2 and R3 in the graded architecture was found to be 73 ± 9 % and 72 ± 4 %, respectively. This was comparable to the porosity of the random architecture (71 ± 4 %). However, the diameter of the struts in R2 and R3 of the graded architecture was approximately 20 % greater than that of the CAD model (see Tables 1 and 2). This was mainly due to the shape of the diamond unit cell and the design procedure we used (graded architectures were created with 100 μm offset between each cell size region to anchor the neighbouring layers with each other and prevent their slipping out, as shown in Fig. S1). The additional material introduced at the

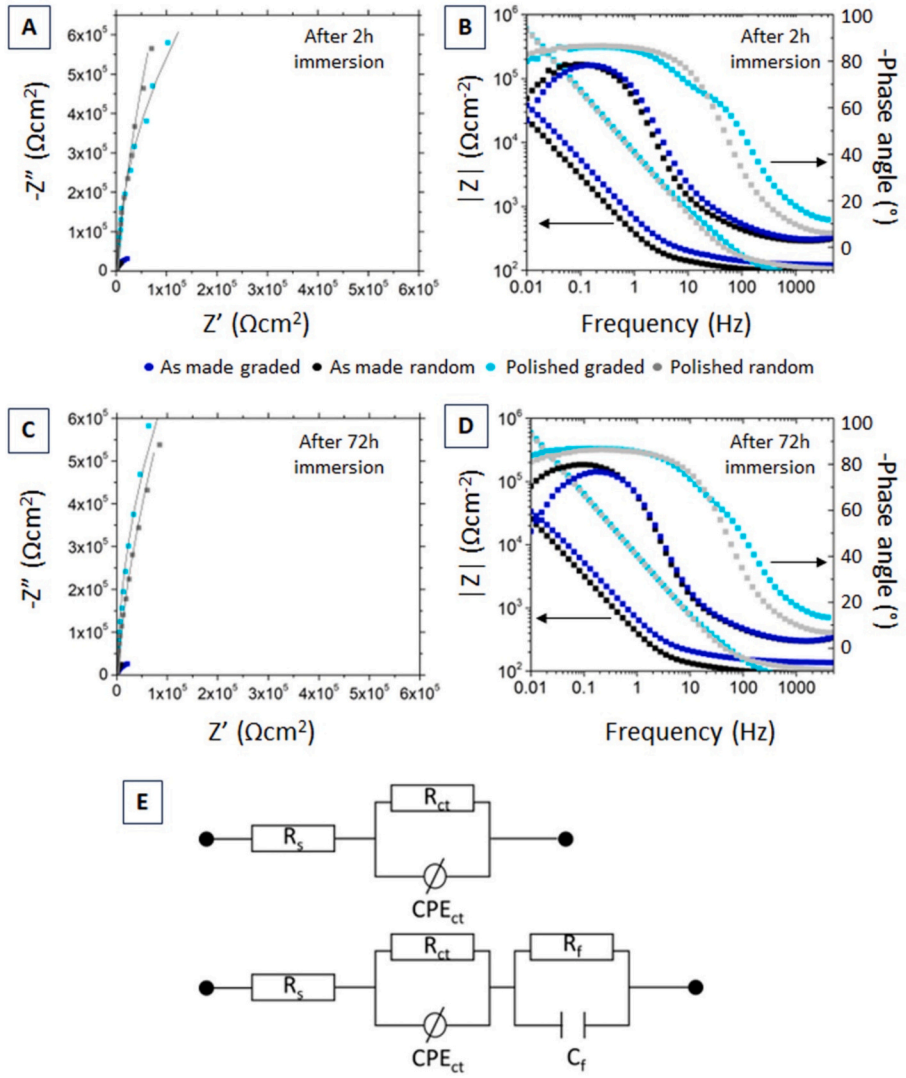


**Fig. 6.** EIS results performed in PBS at 37 °C: a) Nyquist plots recorded after 2 h of immersion, b) Bode plot and phase angle vs frequency recorded after 2 h of immersion, c) Nyquist plots recorded after 72 h of immersion, d) Bode plots and phase angle vs frequency recorded after 72 h of immersion, e) scheme of electrochemical equivalent circuits; upper one for as-made scaffolds and polished random scaffolds, and the lower one for polished graded scaffolds.

**Table 4**
Electrochemical parameters fitted for EIS results based on 3 repetitions (mean ± standard deviation) using the electrochemical equivalent circuit shown in Fig. 6e, where: $R_s$ – resistance of the electrolyte, $R_{ct}$ – resistance of the electric-charge transfer through the material and electrolyte interface, $Y_{ct}$ – capacitance of the double layer at the material-electrolyte interface, $a_1$ – dispersion coefficient of $CPE_{ct}$, $R_f$ – resistance of the film, $C_f$ – capacitance of the film.

| Scaffold | Immersion time | $R_s$ [Ω•cm²] | $R_{ct}$ [kΩ•cm²] | $Y_{ct}$ [x10⁻⁵ S·s^a/cm²] | $a_1$ | $R_f$ [Ω•cm²] | $C_f$ [x10⁻⁵ F/cm²] |
|---|---|---|---|---|---|---|---|
| As made graded | 2 h | 177 ± 3 | 80.5 ± 9.1 | 20 ± 0.1 | 0.92 ± 0.02 | – | – |
| | 72 h | 183 ± 4 | 62.5 ± 11.1 | 30 ± 1.1 | 0.92 ± 0.01 | – | – |
| As made random | 2 h | 129 ± 3 | 72.8 ± 4.2 | 50 ± 3.2 | 0.92 ± 0.02 | – | – |
| | 72 h | 120 ± 3 | 118 ± 11.2 | 40 ± 2.1 | 0.93 ± 0.03 | – | – |
| Polished graded | 2 h | 65 ± 2 | 60 ± 6.0 | 30 ± 2.3 | 0.57 ± 0.04 | 3300 ± 128 | 3 ± 0.1 |
| | 72 h | 53 ± 2 | 88 ± 6.2 | 50 ± 2.6 | 0.50 ± 0.03 | 4800 ± 117 | 3 ± 0.1 |
| Polished random | 2 h | 136 ± 1 | 8670 ± 117.0 | 3 ± 0.01 | 0.96 ± 0.01 | – | – |
| | 72 h | 131 ± 2 | 5870 ± 211.0 | 3 ± 0.02 | 0.96 ± 0.01 | – | – |

100 μm interface region between the zones resulted in the appearance of several thicker struts and an overall decrease in porosity, significantly impacting the statistical analysis of the results by means of μCT algorithms.

### 4.2. Corrosion resistance

It is clear that chemical polishing of the scaffolds after PBF-LB fabrication is crucial for removing residual particles and improving corrosion resistance of the scaffolds. The loosely adherent particles on the surface of the scaffolds increase the surface area, resulting in the acceleration of the corrosion reactions. Moreover, as shown in our

**Table 5**
Polarization resistance ($R_p$) calculated based on EIS fitting shown in Table 4.

| Scaffold | $R_p$ [kΩ•cm$^2$] after 2 h of immersion | $R_p$ [kΩ•cm$^2$] after 72 h of immersion |
|---|---|---|
| As made graded | 81 ± 7 | 63 ± 11 |
| As made random | 73 ± 8 | 118 ± 16 |
| Polished graded | 3360 ± 113 | 4888 ± 121 |
| Polished random | 8670 ± 223 | 5870 ± 196 |

previous work, the chemical state of the Ti surface was altered by chemical polishing [34]. On the surface of the as-made scaffolds, a mixture of $TiO_2$ and metallic Ti was mainly recognized. However, after chemical polishing, primarily $TiO_2$ was observed (suggesting the growth of the $TiO_2$ layer). The presence of the passive $TiO_2$ layer protects the Ti substrate against corrosion. The results of this work show that scaffold architecture had an effect on its corrosion resistance. Similar observations were made by Wei Xu et al., who showed that after 2 h of immersion in PBS, the functionally graded structure design with the average porosity of 20–80 % might enhance corrosion resistance of porous scaffolds [54]. In the mentioned work, there is no information on how the passive film behaved after a longer time of immersion. Our study presented that the passive film of the graded scaffold became more stable than the one formed on the random scaffold when extending the immersion time. After 72 h of immersion, the $R_p$ of the random scaffold was 5870 ± 196 kΩ × cm$^2$, whilst that of the graded scaffold was 4888 ± 121 kΩ × cm$^2$. We believe that those differences stemmed from the local pH changes within interpore areas, which play a detrimental role in the degradation processes of the implant [55]. The local changes in pH within single pores depend on the volume ratio of the solution flowing through the interpore areas; the smaller volume, the greater changes in pH may be denoted. As a result of the occurring reactions, the local acidification may take place which, in turn, limits the formation of stable oxide layer and leads to faster dissolution of Ti [56]. Based on EIS results, it is clear that graded scaffolds supported passivation reactions. The randomly distributed pores did not show any tendency to form an oxide film, which might be related to lowering local pH within interpore areas. Such condition supports dissolution reactions. Nevertheless, those conclusions are made based on the EIS results obtained from experiments conducted in large-volume ratio experimental cells. They must be supported by very specific measurements in small-volume experimental cells, using methods that allow to measurements very small changes in local areas, i.e. scanning electron microscopy techniques (SECM).

### 4.3. Biological performance

The pore distribution in the scaffold also affected the performance of hMSC, and the biggest difference was observed at the first day of culture. As indicated by the DNA measurement, the graded scaffolds retained almost two times more cells than the random ones (Fig. 8A). Moreover, the microscopic observations revealed that the highest concentration of cells was localized in the R1 zone of the top surface (see Fig. 7). This zone was made of the smallest pores, had the smallest porosity and the highest SA/V (see Fig. 3 and Table 2), therefore, it was more favourable for initial cell adhesion. This is consistent with observations reported in our previous studies [7,8] and the one by Van Bael and co-workers [57].

Although the initial cell retention was higher on the graded scaffolds, the hMSC proliferation was significantly higher on the random scaffolds (as depicted in Fig. 8C). This finding could be explained by the localized, high initial cell density in the scaffold. On the graded scaffolds, the majority of the cells were concentrated within the R1 zone. Consequently, they reached confluency already after the first day of culture (as

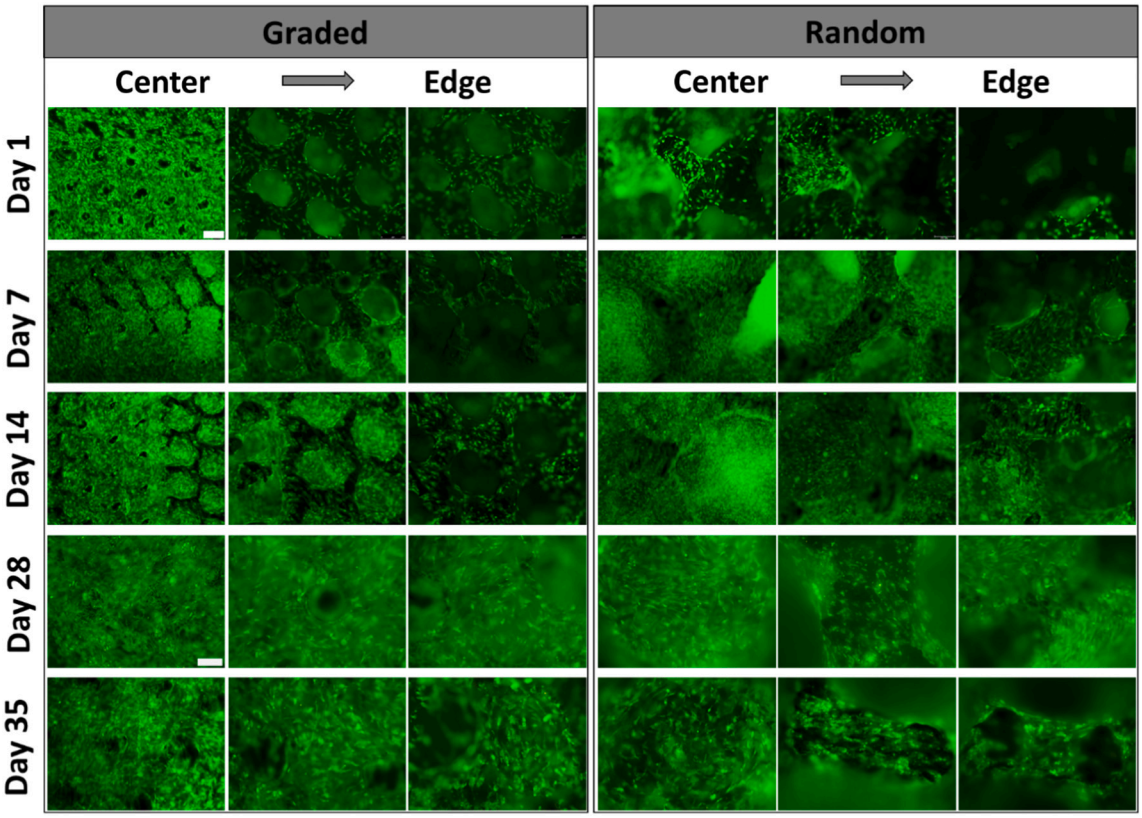


**Fig. 7.** Live/dead stain of hMSC cultured on the Ti scaffolds with random and graded architecture for up to five weeks. Green – all cells; red – dead cells. Scale bar 200 μm.

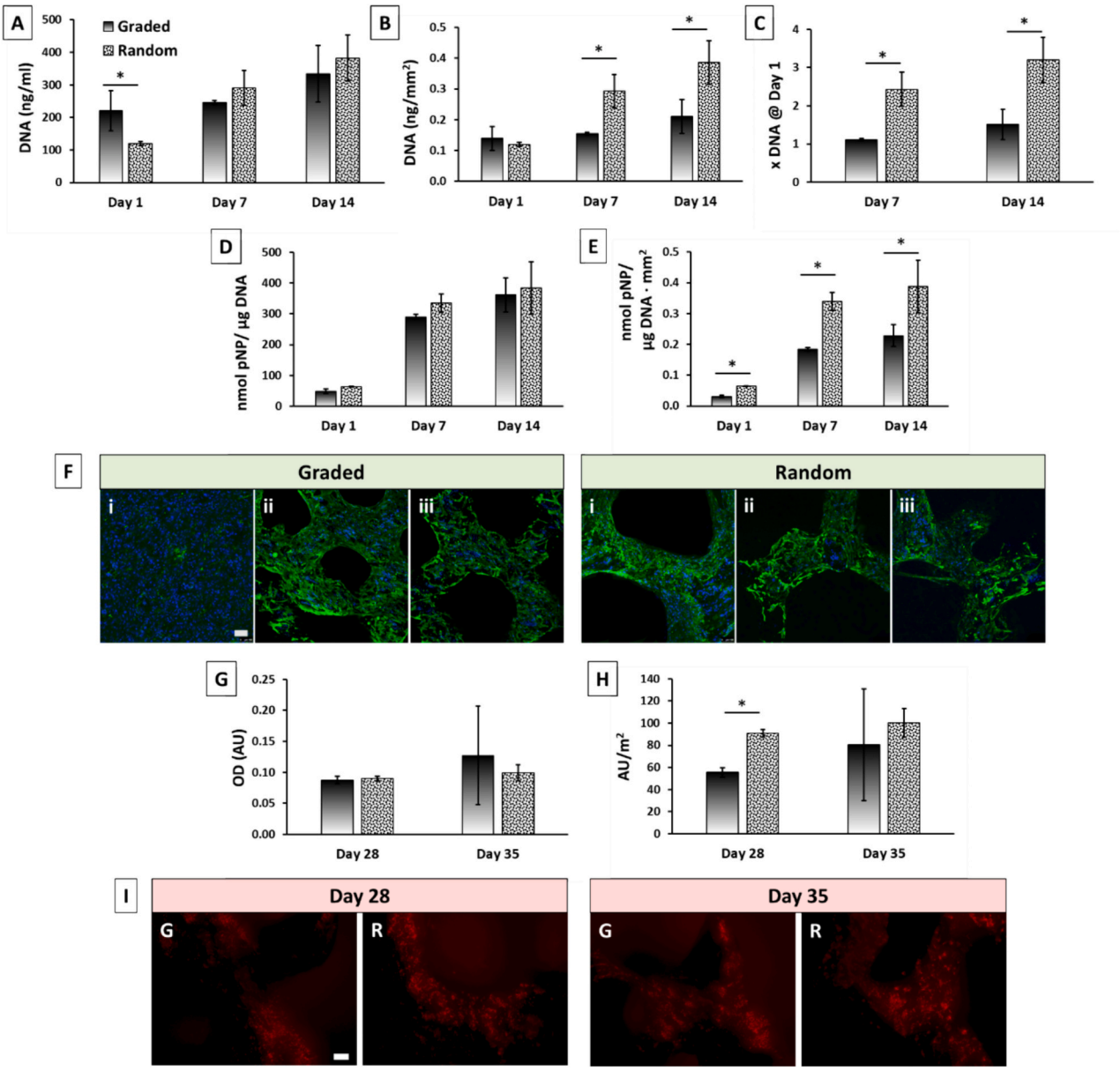


**Fig. 8.** Effect of the graded and random architecture of the scaffolds on cell proliferation and differentiation. (A) Cell proliferation determined as DNA concentration over 14 days of culture. Cell proliferation was normalized to the surface area of the scaffolds (B) and to day 1 (C). HMSC osteogenic differentiation was determined by ALP activity (D, E) and ALP expression (F), and by quantitative (G, H) and qualitative (I) analysis of mineralization. ALP activity and mineralization were normalized to the surface area of the scaffolds (E, H). AU – arbitrary units; * - $p < 0.05$. (F) Visualisation of ALP expression by immunocytochemical staining at day 7. The ALP expression (green) was lower in the areas with higher cell density (blue nuclei); i – centre of the scaffolds, ii – intermediate zone, iii – outer zone. (I) Fluorescent labelling of calcium deposits at day 28 and day 35. Mineralization (red) was visible in the outer region of the graded (G) and the random (R) scaffolds. Scale bar 100 µm.

shown in Fig. 7). This, in turn, led to lower proliferation rate due to the contact inhibition phenomenon [58]. On the other hand, the lower initial cell density on the random scaffolds (on the top surface, as seen Fig. 7) allowed for more space for proliferation, despite the nearly 30 % lower surface area of the random scaffolds. Moreover, the random scaffolds had the higher volume content of pores with a diameter $\geq$ 500 µm than the graded scaffolds (62 $\pm$ 7 % and 19 $\pm$ 4 %, respectively; see Fig. 4), which could enable better nutrient diffusion for cell growth and differentiation. In contrast, the smallest pores of the graded scaffolds became occluded by cells after 1 week of culture, further hindering the diffusion. Onal and co-workers measured better proliferation of MC3T3-E1 preosteoblast cells on the outside surface of both homogeneous scaffolds with larger pores and graded scaffolds with larger pores on their outside surface [28]. Better cell proliferation on homogenous scaffolds with larger pores was also reported by other groups [59–61].

The cell density also affected the expression of ALP. As demonstrated by immunocytochemical staining, ALP-positive cells were predominantly found in areas with lower cell densities, i.e., in the outer regions of the investigated scaffolds. The struts in the R3 zone of the graded scaffolds had similar diameter to those in the graded scaffolds, and were 45 % higher than the struts in the R1 zone. Consequently, this led to a lower SA/V, allowing cells to assume a more polygonal shape rather than the fibroblast-associated spindle-like shape. These findings align with McBeath and co-authors' research, which demonstrated that hMSC differentiated into osteoblasts when they have a higher surface area available for their spreading, as well as at lower seeding densities [62].

The mineralization nodules were also predominantly localized in the outer regions of the scaffolds. The improved mineralization occurring in

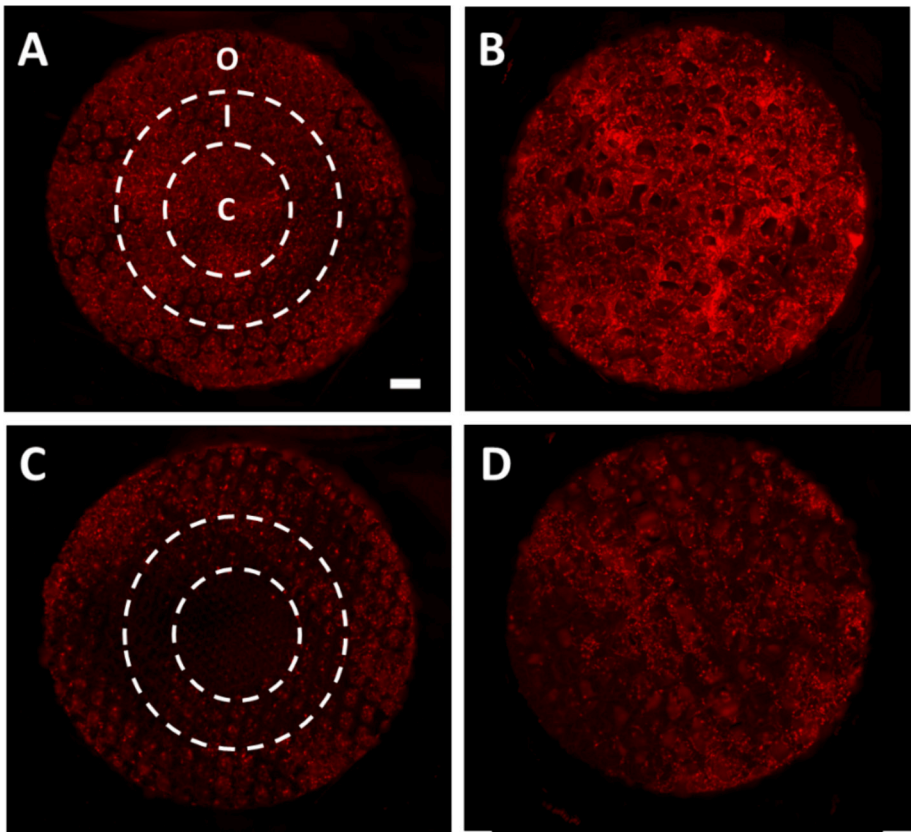


**Fig. 9.** Colonization of graded (A, C) and random (B, D) scaffolds by hMSC migrating out of monolayer placed on top of the scaffolds after 14 days in culture. The hMSC colonized the top surface of both types of the scaffolds (A, B), outer zone of the bottom side of the graded scaffolds (C) and most of the bottom side of the random scaffolds (D). The dashed lines represent different zones of the graded architecture: C –core, I – intermediate and O – outer zone. Scale bar = 1 mm.

these outer regions could be attributed to their higher porosity. Specifically, the R2 and R3 zones of the graded scaffolds exhibited porosity similar that of the random ones (approximately 70 %). This porosity, combined with the absence of pores occluded by cells, should facilitate better diffusion of nutrients and acidic metabolites. In our previous study, we demonstrated that deposition of calcium phosphates in 3D composite scaffolds is hindered by presence of acidic degradation products [63]. In summary, we believe that the enhanced osteogenic differentiation in the outer regions of the scaffolds resulted from a lower initial cell density and a lower SA/V, both of which allowed for better cell spreading, as well as the higher porosity, which enabled better removal of acidic metabolic waste.

Since the scaffolds investigated in the present study had different surface areas, this parameter had to be taken into account in the analysis of cell performance. In this instance, the random architecture outperformed the graded one. Van Bael and co-workers observed improved cell proliferation on the scaffolds with higher diffusivity, however, contrary to our findings, they did not find any significant effect on ALP activity [57]. The group, however, investigated the scaffolds with homogenous pores. This might suggest the benefit of random distribution of pores with different pore sizes for osteogenic differentiation of stem cells. Another possible explanation of the improved osteogenic differentiation of hMSC on the random scaffolds could be attributed to its lower surface area arose from the thicker struts incorporated into the scaffold design; as demonstrated by Perier-Metz and co-workers by in silico modelling, thicker struts were favourable for bone development [64].

In order to simulate cell migration from the surrounding tissue under implantation conditions, we performed an experiment using the hMSC monolayer placed on the top surface of the scaffolds. Such experimental setup enables to measure cellular colonization of the scaffolds. We observed qualitative differences in colonization at the bottom surface of the scaffolds; a complete coverage of the bottom surface of the random scaffolds vs. a lack of hMSC in R1 of the graded scaffolds (see Fig. 9). However, the quantitative analysis (see Fig. 10) did not reveal any significant differences between the two types of scaffolds, suggesting that the architecture affected the rate of cell migration throughout the scaffold but not the total number of the cells migrating into it. The similar cell number could be a result of the higher surface area of the graded scaffolds being in contact with the cell monolayer, and the lower surface area coupled with the higher diffusivity of the random scaffolds leading to the higher migration rate of hMSC. Kato and co-workers determined that an optimal balance between the pore size and the surface area available for cell transfer from the silicone sheet is required for efficient cell migration through the scaffolds; larger pores foster cell migration but simultaneously reduce the opportunity of cell transfer [45]. On the other hand, R1 of the graded scaffolds had the smallest strut thickness and the highest SA/V (see Table 2); these parameters were reported to reduce cellular migration [64]. Lower migration of hMSC within R1 of the graded scaffolds could also results from its lower porosity, which hiders the nutrient diffusion and creates hypoxic conditions [30]. This could be supported by other studies, which used cell suspensions, indicating that the areas with larger pores had better conditions for cells growth [8,28,65]. The hMSC performance in the "monolayer experiment" was also significantly better on the random architecture than graded one, when the total DNA content, metabolic, and ALP activities were normalized to the scaffold surface area. As indicated by Van Bael and co-workers, this could be due to better diffusivity of the random architecture having higher fraction of pores $\geq$500 μm [57]. Interestingly, the higher cellular colonization of the scaffolds with a higher fraction of larger pores, thicker struts, and higher SA/V, is consistent with the higher in vivo bone regeneration in scaffold

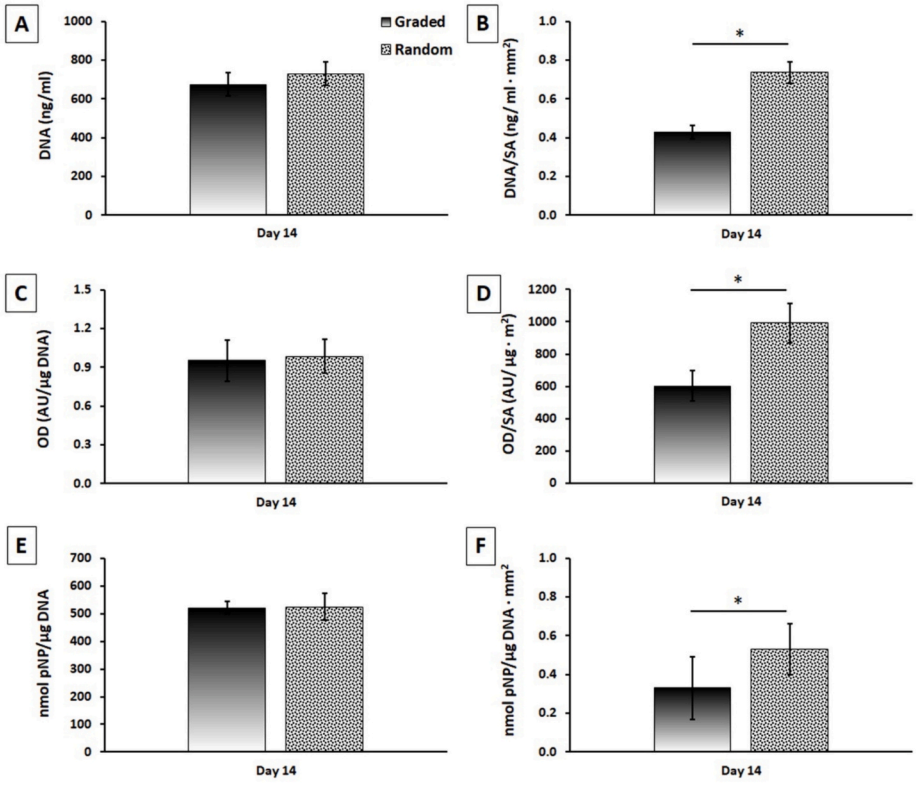


**Fig. 10.** Quantification of the colonization of the scaffolds by hMSC migrating from the cell monolayer placed on the scaffolds. A) Total DNA content, B) total DNA content normalized to the scaffold surface area (SA), C) metabolic activity determined by means of MTS assay normalized to the total DNA content, D) metabolic activity normalized to the total DNA content per the SA, E) ALP activity and F) ALP activity normalized to the SA. * - $p < 0.05$.

with these features [61,66]. Therefore, the monolayer setup seems to be an interesting tool for in vitro screening of 3D porous scaffolds for potential bone regeneration properties.

## 5. Conclusion

The PBF-LB process allowed for fabricating the scaffold for tissue engineering with graded and randomly distributed pores having diameters of 200 to 700 µm. The chemical polishing process successfully removed unmelted powder particles from the entire surface and interior of the scaffolds. The structures obtained in our study closely represented their CAD models, with an average porosity decrease of 5 %.

The chemical polishing improved the corrosion resistance of both graded and random scaffolds significantly. The distribution of the pores influenced the corrosion mechanism of the scaffolds. The passive film on the graded scaffolds increased its stability with increase in immersion time, whereas that on the random scaffold decreased.

The distribution of pores affected the distribution of hMSC in the scaffolds; smaller pores of the graded architecture entrapped more cells. The osteogenic differentiation was enhanced in the outer regions of both types of scaffolds, which had similar strut thickness and porosity. Additionally, the scaffolds with the random architecture outperformed the graded ones with respect to hMSC proliferation, differentiation and migration when normalized to the scaffold surface area.

In this study, the similar porosity of both scaffolds was achieved at the expense of the strut thickness and different fractions of pore sizes. Therefore, it was impossible to isolate a single underlying cause for the improved performance of the random architecture. Nevertheless, these results indicate the possibility of improving bone regeneration through the architectural design of 3D scaffolds that combine random distribution of pores with varying diameters.

Supplementary data to this article can be found online at https://doi.org/10.1016/j.bioadv.2024.213955.

## CRediT authorship contribution statement

**J. Idaszek:** Writing – review & editing, Writing – original draft, Methodology, Investigation, Formal analysis. **B. Wysocki:** Writing – review & editing, Writing – original draft, Methodology, Investigation, Formal analysis. **E. Ura-Bińczyk:** Methodology, Investigation, Formal analysis. **A. Dobkowska:** Writing – review & editing, Writing – original draft, Methodology, Investigation, Formal analysis. **W. Nowak:** Methodology, Investigation, Formal analysis. **A. Yamamoto:** Writing – original draft, Supervision, Methodology, Funding acquisition, Conceptualization. **G.D. Sulka:** Writing – original draft, Supervision, Resources, Funding acquisition, Conceptualization. **W. Święszkowski:** Writing – original draft, Supervision, Resources, Funding acquisition, Conceptualization.

## Declaration of competing interest

The authors declare that they have no known competing financial interests or personal relationships that could have appeared to influence the work reported in this paper.

## Data availability

Data will be made available on request.

## Acknowledgements

The authors would like to thank the NCN (National Science Center) for providing financial support to project Synthesis and characterization of novel biomaterials based on 3D multifunctional titanium substrates (Grant No. 2017/25/B/ST8/01599).

The Authors would like to acknowledge Jakub Skibiński, PhD Eng., who created the CAD designs of scaffolds with randomly distributed

pores.

## References


[1] R. Lanza, R. Langer, J.P. Vacanti, A. Atala, Principles of Tissue Engineering, 5th ed., Elsevier, 2020 https://doi.org/10.1016/C2018-0-03818-9.

[2] A. Haleem, M. Javaid, R.H. Khan, R. Suman, 3D printing applications in bone tissue engineering, J. Clin. Orthop. Trauma 11 (Feb. 2020) S118–S124, https://doi.org/10.1016/J.JCOT.2019.12.002.

[3] D.S. Musgrave, F.H. Fu, J. Huard, Gene therapy and tissue engineering in orthopaedic surgery, J. Am. Acad. Orthop. Surg. 10 (1) (2002) 6–15, https://doi.org/10.5435/00124635-200201000-00003.

[4] E. Jabbarzadeh, et al., Induction of angiogenesis in tissue-engineered scaffolds designed for bone repair: a combined gene therapy–cell transplantation approach, Proc. Natl. Acad. Sci. 105 (32) (Aug. 2008) 11099–11104, https://doi.org/10.1073/PNAS.0800069105.

[5] C. Han, et al., Continuous functionally graded porous titanium scaffolds manufactured by selective laser melting for bone implants, J. Mech. Behav. Biomed. Mater. 80 (Apr. 2018) 119–127, https://doi.org/10.1016/J.JMBBM.2018.01.013.

[6] S. Zhao, et al., Compressive and fatigue behavior of functionally graded Ti-6Al-4V meshes fabricated by electron beam melting, Acta Mater. 150 (May 2018) 1–15, https://doi.org/10.1016/J.ACTAMAT.2018.02.060.

[7] B. Wysocki, et al., Post processing and biological evaluation of the titanium scaffolds for bone tissue engineering, Materials *9* (3) (Mar. 2016) *197*, https://doi.org/10.3390/MA9030197.

[8] B. Wysocki, et al., The influence of chemical polishing of titanium scaffolds on their mechanical strength and in-vitro cell response, Mater. Sci. Eng. C 95 (Feb. 2019) 428–439, https://doi.org/10.1016/J.MSEC.2018.04.019.

[9] A.S. Mao, J.W. Shin, D.J. Mooney, Effects of substrate stiffness and cell-cell contact on mesenchymal stem cell differentiation, Biomaterials 98 (Aug. 2016) 184–191, https://doi.org/10.1016/J.BIOMATERIALS.2016.05.004.

[10] R.A. Perez, G. Mestres, Role of pore size and morphology in musculo-skeletal tissue regeneration, Mater. Sci. Eng. C 61 (Apr. 2016) 922–939, https://doi.org/10.1016/J.MSEC.2015.12.087.

[11] V.K. Balla, S. Bodhak, S. Bose, A. Bandyopadhyay, Porous tantalum structures for bone implants: fabrication, mechanical and in vitro biological properties, Acta Biomater. 6 (8) (Aug. 2010) 3349–3359, https://doi.org/10.1016/J.ACTBIO.2010.01.046.

[12] B. Dabrowski, W. Swieszkowski, D. Godlinski, K.J. Kurzydlowski, Highly porous titanium scaffolds for orthopaedic applications, J. Biomed. Mater. Res. B Appl. Biomater. 95B (1) (Oct. 2010) 53–61, https://doi.org/10.1002/JBM.B.31682.

[13] A. Ataee, Y. Li, M. Brandt, C. Wen, Ultrahigh-strength titanium gyroid scaffolds manufactured by selective laser melting (SLM) for bone implant applications, Acta Mater. 158 (Oct. 2018) 354–368, https://doi.org/10.1016/J.ACTAMAT.2018.08.005.

[14] J.H. Ahn, et al., 3D-printed biodegradable composite scaffolds with significantly enhanced mechanical properties via the combination of binder jetting and capillary rise infiltration process, Addit. Manuf. 41 (May 2021) 101988, https://doi.org/10.1016/J.ADDMA.2021.101988.

[15] D. Barba, E. Alabort, R.C. Reed, Synthetic bone: design by additive manufacturing, Acta Biomater. 97 (Oct. 2019) 637–656, https://doi.org/10.1016/J.ACTBIO.2019.07.049.

[16] Y. Chen, W. Li, C. Zhang, Z. Wu, J. Liu, Recent developments of biomaterials for additive manufacturing of bone scaffolds, Adv. Healthc. Mater. 9 (23) (Dec. 2020) 2000724, https://doi.org/10.1002/ADHM.202000724.

[17] B.A. Wysocki, et al., Mechanical properties of Ti grade 2 manufactured using laser beam powder bed fusion (PBF-LB) with checkerboard laser scanning and in situ oxygen strengthening, Crystals 14 (6) (Jun. 2024) 574, https://doi.org/10.3390/CRYST14060574.

[18] Y. Qin, et al., Additive manufacturing of biodegradable metals: current research status and future perspectives, Acta Biomater. 98 (Oct. 2019) 3–22, https://doi.org/10.1016/J.ACTBIO.2019.04.046.

[19] C. Ling, et al., Influence of heat treatment on microstructure, mechanical and corrosion behavior of WE43 alloy fabricated by laser-beam powder bed fusion, Int. J. Extreme Manuf. 6 (1) (Oct. 2023) 015001, https://doi.org/10.1088/2631-7990/ACFAD5.

[20] Y. Yang, et al., Microstructure development and biodegradation behavior of additively manufactured Mg-Zn-Gd alloy with LPSO structure, J. Mater. Sci. Technol. 144 (0) (May 2023) 1–14, https://doi.org/10.1016/j.jmst.2022.09.059.

[21] C. Zhang, D. Ouyang, S. Pauly, L. Liu, 3D printing of bulk metallic glasses, Mater. Sci. Eng. R. Rep. 145 (Jul. 2021) 100625, https://doi.org/10.1016/J.MSER.2021.100625.

[22] Ł. Żrodowski, et al., How to control the crystallization of metallic glasses during laser powder bed fusion? Towards part-specific 3D printing of in situ composites, Addit. Manuf. 76 (Aug. 2023) 103775, https://doi.org/10.1016/J.ADDMA.2023.103775.

[23] J. Fu, S. Qu, J. Ding, X. Song, M.W. Fu, Comparison of the microstructure, mechanical properties and distortion of stainless steel 316 L fabricated by micro and conventional laser powder bed fusion, Addit. Manuf. 44 (Aug. 2021) 102067, https://doi.org/10.1016/J.ADDMA.2021.102067.

[24] Z. Hu, et al., Micro laser powder bed fusion of stainless steel 316L: cellular structure, grain characteristics, and mechanical properties, Mater. Sci. Eng. A 848 (Jul. 2022) 143345, https://doi.org/10.1016/J.MSEA.2022.143345.

[25] A. Chmielewska, B.A. Wysocki, Ł. Żrodowski, W. Święszkowski, Hybrid solid-porous titanium scaffolds: fabrication and post processing after selective laser melting, Trans. AMMM 1 (1) (Sep. 2019) 2–3, https://doi.org/10.18416/AMMM.2019.1909S10T02.

[26] V. Karageorgiou, D. Kaplan, Porosity of 3D biomaterial scaffolds and osteogenesis, Biomaterials 26 (27) (Sep. 2005) 5474–5491, https://doi.org/10.1016/J.BIOMATERIALS.2005.02.002.

[27] X. Wang, et al., Topological design and additive manufacturing of porous metals for bone scaffolds and orthopaedic implants: a review, Biomaterials 83 (Mar. 2016) 127–141, https://doi.org/10.1016/J.BIOMATERIALS.2016.01.012.

[28] E. Onal, J.E. Frith, M. Jurg, X. Wu, A. Molotnikov, Mechanical Properties and In Vitro Behavior of Additively Manufactured and Functionally Graded Ti6Al4V Porous Scaffolds, Metals 8 (4) (Mar. 2018) 200, https://doi.org/10.3390/MET8040200.

[29] A. Di Luca, et al., Tuning cell differentiation into a 3D scaffold presenting a pore shape gradient for osteochondral regeneration, Adv. Healthc. Mater. 5 (14) (Jul. 2016) 1753–1763, https://doi.org/10.1002/ADHM.201600083.

[30] A. Di Luca, et al., Gradients in pore size enhance the osteogenic differentiation of human mesenchymal stromal cells in three-dimensional scaffolds, Sci. Rep. 6 (1) (Mar. 2016) 1–13, https://doi.org/10.1038/srep22898.

[31] A. Di Luca, et al., Influencing chondrogenic differentiation of human mesenchymal stromal cells in scaffolds displaying a structural gradient in pore size, Acta Biomater. 36 (May 2016) 210–219, https://doi.org/10.1016/J.ACTBIO.2016.03.014.

[32] N. Taniguchi, et al., Effect of pore size on bone ingrowth into porous titanium implants fabricated by additive manufacturing: an in vivo experiment, Mater. Sci. Eng. C 59 (Feb. 2016) 690–701, https://doi.org/10.1016/J.MSEC.2015.10.069.

[33] S.C.P. Cachinho, R.N. Correia, Titanium scaffolds for osteointegration: mechanical, in vitro and corrosion behaviour, J. Mater. Sci. Mater. Med. 19 (1) (Jan. 2008) 451–457, https://doi.org/10.1007/S10856-006-0052-7.

[34] B. Wysocki, et al., The influence of selective laser melting (SLM) process parameters on in-vitro cell response, Int. J. Mol. Sci. 19 (6) (May 2018) 1619, https://doi.org/10.3390/IJMS19061619.

[35] B. Łosiewicz, J. Maszybrocka, J. Kubisztal, G. Skrabalak, A. Stwora, Corrosion Resistance of the CpTi G2 Cellular Lattice with TPMS Architecture for Gas Diffusion Electrodes, Materials 14 (1) (Dec. 2020) 81, https://doi.org/10.3390/MA14010081.

[36] T. Puttonen, S. Chekurov, J. Kuva, R. Björkstrand, J. Partanen, M. Salmi, Influence of feature size and shape on corrosion of 316L lattice structures fabricated by laser powder bed fusion, Addit. Manuf. 61 (Jan. 2023) 103288, https://doi.org/10.1016/J.ADDMA.2022.103288.

[37] A. du Plessis, et al., Properties and applications of additively manufactured metallic cellular materials: a review, Prog. Mater. Sci. 125 (Apr. 2022) 100918, https://doi.org/10.1016/J.PMATSCI.2021.100918.

[38] D. Westhoff, J. Skibinski, O. Šedivý, B. Wysocki, T. Wejrzanowski, V. Schmidt, Investigation of the relationship between morphology and permeability for open-cell foams using virtual materials testing, Mater. Des. 147 (Jun. 2018) 1–10, https://doi.org/10.1016/J.MATDES.2018.03.022.

[39] J. Skibinski, K. Cwieka, T. Kowalkowski, B. Wysocki, T. Wejrzanowski, K. J. Kurzydlowski, The influence of pore size variation on the pressure drop in open-cell foams, Mater. Des. 87 (Dec. 2015) 650–655, https://doi.org/10.1016/J.MATDES.2015.08.079.

[40] B. Shaqour, et al., Novel design for an additively manufactured nozzle to produce tubular scaffolds via fused filament fabrication, Addit. Manuf. 49 (Jan. 2022) 102467, https://doi.org/10.1016/J.ADDMA.2021.102467.

[41] B. Wysocki, P. Maj, R. Sitek, J. Buhagiar, K.J. Kurzydłowski, W. Święszkowski, Laser and electron beam additive manufacturing methods of fabricating titanium bone implants, Appl. Sci. 7 (7) (Jun. 2017) 657, https://doi.org/10.3390/APP7070657.

[42] B. Wysocki, et al., Microstructure and mechanical properties investigation of CP titanium processed by selective laser melting (SLM), J. Mater. Process. Technol. 241 (Mar. 2017) 13–23, https://doi.org/10.1016/J.JMATPROTEC.2016.10.022.

[43] A. Chmielewska, A. Jahadakbar, B. Wysocki, M. Elahinia, W. Święszkowski, D. Dean, Chemical polishing of additively manufactured, porous, nickel-titanium skeletal fixation plates, 3D Print. Addit. Manuf. 9 (4) (Aug. 2022) 269–277, https://doi.org/10.1089/3DP.2020.0209/ASSET/IMAGES/LARGE/3DP.2020.0209_FIGURE5.JPEG.

[44] B. Wysocki, et al., Method for additive production of three-dimensional objects, PL 233190 (2019).

[45] K. Kato, et al., Novel multilayer Ti foam with cortical bone strength and cytocompatibility, Acta Biomater. 9 (3) (Mar. 2013) 5802–5809, https://doi.org/10.1016/J.ACTBIO.2012.11.018.

[46] C.M. Stanford, P.A. Jacobson, E.D. Eanes, L.A. Lembke, R.J. Midura, Rapidly forming apatitic mineral in an osteoblastic cell line (UMR 106—01 BSP), J. Biol. Chem. 270 (16) (Apr. 1995) 9420–9428, https://doi.org/10.1074/JBC.270.16.9420.

[47] T. Goto, H. Kajiwara, M. Yoshinari, E. Fukuhara, S. Kobayashi, T. Tanaka, In vitro assay of mineralized-tissue formation on titanium using fluorescent staining with calcein blue, Biomaterials 24 (22) (Oct. 2003) 3885–3892, https://doi.org/10.1016/S0142-9612(03)00258-8.

[48] Y.H. Wang, Y. Liu, P. Maye, D.W. Rowe, Examination of mineralized nodule formation in living osteoblastic cultures using fluorescent dyes, Biotechnol. Prog. 22 (6) (Nov. 2006) 1697–1701, https://doi.org/10.1021/BP060274B.

[49] I. Milošev, T. Kosec, H.H. Strehblow, XPS and EIS study of the passive film formed on orthopaedic Ti–6Al–7Nb alloy in Hank's physiological solution, Electrochim.

Acta 53 (9) (Mar. 2008) 3547–3558, https://doi.org/10.1016/J.ELECTACTA.2007.12.041.
[50] A. Asserghine, D. Filotás, B. Németh, L. Nagy, G. Nagy, Potentiometric scanning electrochemical microscopy for monitoring the pH distribution during the self-healing of passive titanium dioxide layer on titanium dental root implant exposed to physiological buffered (PBS) medium, Electrochem. Commun. 95 (Oct. 2018) 1–4, https://doi.org/10.1016/J.ELECOM.2018.08.008.
[51] A.D. King, N. Birbilis, J.R. Scully, Accurate electrochemical measurement of magnesium corrosion rates; a combined impedance, mass-loss and hydrogen collection study, Electrochim. Acta 121 (Mar. 2014) 394–406, https://doi.org/10.1016/J.ELECTACTA.2013.12.124.
[52] R.G. Kelly, J.R. Scully, D. Shoesmith, R.G. Buchheit, Electrochemical Techniques in Corrosion Science and Engineering, 1st ed., CRC Press, 2002 https://doi.org/10.1201/9780203909133.
[53] A. Dobkowska, et al., A comparison of the corrosion behaviour of copper materials in dilute nitric acid, Corros. Sci. 192 (Nov. 2021) 109778, https://doi.org/10.1016/J.CORSCI.2021.109778.
[54] W. Xu, et al., Gyroid-based functionally graded porous titanium scaffolds for dental application: design, simulation and characterizations, Mater. Des. 224 (Dec. 2022) 111300, https://doi.org/10.1016/J.MATDES.2022.111300.
[55] A. Asserghine, D. Filotás, B. Németh, L. Nagy, G. Nagy, Potentiometric scanning electrochemical microscopy for monitoring the pH distribution during the self-healing of passive titanium dioxide layer on titanium dental root implant exposed to physiological buffered (PBS) medium, Electrochem. Commun. 95 (Oct. 2018) 1–4, https://doi.org/10.1016/J.ELECOM.2018.08.008.
[56] A. Sharma, M.C. Oh, J.T. Kim, A.K. Srivastava, B. Ahn, Investigation of electrochemical corrosion behavior of additive manufactured Ti–6Al–4V alloy for medical implants in different electrolytes, J. Alloys Compd. 830 (Jul. 2020) 154620, https://doi.org/10.1016/J.JALLCOM.2020.154620.
[57] S. Van Bael, et al., The effect of pore geometry on the in vitro biological behavior of human periosteum-derived cells seeded on selective laser-melted Ti6Al4V bone scaffolds, Acta Biomater. 8 (7) (Jul. 2012) 2824–2834, https://doi.org/10.1016/J.ACTBIO.2012.04.001.
[58] M.F. Pittenger, D.E. Discher, B.M. Péault, D.G. Phinney, J.M. Hare, A.I. Caplan, Mesenchymal stem cell perspective: cell biology to clinical progress, npj Regener. Med. 4 (1) (Dec. 2019) 1–15, https://doi.org/10.1038/s41536-019-0083-6.
[59] J.P. St-Pierre, M. Gauthier, L.P. Lefebvre, M. Tabrizian, Three-dimensional growth of differentiating MC3T3-E1 pre-osteoblasts on porous titanium scaffolds, Biomaterials 26 (35) (Dec. 2005) 7319–7328, https://doi.org/10.1016/J.BIOMATERIALS.2005.05.046.
[60] M. Domingos, et al., The first systematic analysis of 3D rapid prototyped poly (ε-caprolactone) scaffolds manufactured through BioCell printing: the effect of pore size and geometry on compressive mechanical behaviour and in vitro hMSC viability, Biofabrication 5 (4) (Nov. 2013) 045004, https://doi.org/10.1088/1758-5082/5/4/045004.
[61] B. Chang, et al., Influence of pore size of porous titanium fabricated by vacuum diffusion bonding of titanium meshes on cell penetration and bone ingrowth, Acta Biomater. 33 (Mar. 2016) 311–321, https://doi.org/10.1016/J.ACTBIO.2016.01.022.
[62] R. McBeath, D.M. Pirone, C.M. Nelson, K. Bhadriraju, C.S. Chen, Cell shape, cytoskeletal tension, and RhoA regulate stem cell lineage commitment, Dev. Cell 6 (4) (Apr. 2004) 483–495, https://doi.org/10.1016/S1534-5807(04)00075-9.
[63] J. Idaszek, A. Bruinink, W. Święszkowski, Delayed degradation of poly(lactide-co-glycolide) accelerates hydrolysis of poly(ε-caprolactone) in ternary composite scaffolds, Polym. Degrad. Stab. 124 (Feb. 2016) 119–127, https://doi.org/10.1016/J.POLYMDEGRADSTAB.2015.12.020.
[64] C. Perier-Metz, A. Cipitria, D.W. Hutmacher, G.N. Duda, S. Checa, An in silico model predicts the impact of scaffold design in large bone defect regeneration, Acta Biomater. 145 (Jun. 2022) 329–341, https://doi.org/10.1016/J.ACTBIO.2022.04.008.
[65] T. Mygind, et al., Mesenchymal stem cell ingrowth and differentiation on coralline hydroxyapatite scaffolds, Biomaterials 28 (6) (Feb. 2007) 1036–1047, https://doi.org/10.1016/J.BIOMATERIALS.2006.10.003.
[66] Y. Zheng, Q. Han, J. Wang, D. Li, Z. Song, J. Yu, Promotion of osseointegration between implant and bone interface by titanium alloy porous scaffolds prepared by 3D printing, ACS Biomater. Sci. Eng. 6 (9) (Sep. 2020) 5181–5190, https://doi.org/10.1021/ACSBIOMATERIALS.0C00662/ASSET/IMAGES/LARGE/AB0C00662_0006.JPEG.